RESEARCH ARTICLE

Journal
American Ceramic Society

Cold sintering of bioglass and bioglass/polymer composites

Jessica Andrews[1] | George Bullock[2] | Cheryl A. Miller[2] | Jonathan Booth[3] | Hong Ren[3] | Nicole L. Kelly[4] | John V. Hanna[4,5] | Ian M. Reaney[1]

[1]Materials Science and Engineering, University of Sheffield, Sheffield, UK

[2]School of Clinical Dentistry, University of Sheffield, Sheffield, UK

[3]Johnson Matthey Technology Centre, Reading, UK

[4]Department of Physics, University of Warwick, Coventry, UK

[5]School of Materials Science & Engineering, Nanyang Technological University, Singapore, Republic of Singapore

Correspondence
Jessica Andrews, Materials Science and Engineering, University of Sheffield, Sheffield S1 3JD, UK.
Email: Jessica.andrews@sheffield.ac.uk

Funding information
EPSRC Centre for Doctoral Training in Molecular Analytical Science, Grant/Award Number: EP/L015307/1; EPSRC, Grant/Award Numbers: EP/M028186/1, EP/K024418/1; Advantage West Midlands (AWM); European Regional Development Fund (ERDF); Engineering and Physical Sciences Research Council, Grant/Award Numbers: EP/K024418/1, EP/L015307/1, EP/M028186/1

Abstract
Bioactive glasses are widely utilized to regenerate bone tissue and aid bonding of orthopedic implants. Forming composites of bioglass with bioactive polymers allow the mechanical properties and biological response to be tailored. Although several methods for creating bioglass–polymer composites exist, they require dissolution of the polymer, controlled phase separation, and appear to have an upper limit of ∼30 vol.% bioglass. Cold sintering is a novel technique for the densification of ceramics and glasses which utilizes a liquid phase and pressure to allow the production of components at reduced temperatures. We demonstrate that cold sintering (100°C) of Bioglass 45S5 powder produced via flame spray pyrolysis and the fabrication of Bioglass 45S5–polymer composites. Assessment of the in vitro response revealed that composites were not cytotoxic. Solid-state ^{31}P and ^{29}Si MAS NMR studies of the silicon and phosphorus speciation in the glass powder, as-received, wetted, and sintered samples show similarities to reactions expected when bioglass is implanted in the body which along with Raman spectroscopy data gave insight into the cold sintering densification mechanism.

KEYWORDS
bioactive glass, biocompatibility, composites, low temperature, sinter/sintering

1 | INTRODUCTION

All materials implanted into living tissues elicit some form of response such as tissue death if the material is toxic; replacement of implanted tissue if the material is both nontoxic and soluble; formation of a fibrous tissue capsule if the materials are nontoxic and biologically inactive; and formation of an interfacial bond if the material is nontoxic and biologically active.[1,2] Various materials are used in biomedical applications, including metals, ceramics, polymers, coatings, and composites thereof.[3] The human body is complex with a range of pH within bodily fluids and cyclic stresses applied to bones, joints, and soft tissues.[3] Materials used in biomedical implants should ideally cause

no adverse response once implanted and have mechanical properties compatible with the surrounding tissues.[4]

Bone is a natural, hierarchical composite material which exhibits complex anisotropic mechanical behavior due to structural heterogeneity.[5,6] The mechanical properties of human bone vary between trabecular (spongy) and cortical bone and differ significantly from those of, for example, Bioglass 45S5.[7] Bioactive glasses, such as Bioglass 45S5, are designed to enable the formation of interfacial bonds with surrounding bone tissues and are used to improve fixation of orthopedic implants, in turn improving the expected lifetime of an implant.[8,9] Bioglass 45S5 consists of SiO_2 (45 wt.%), CaO (24.5 wt.%), Na_2O (24.5 wt.%), and P_2O_5 (6 wt.%).[10] A silica-CaO/P_2O_5-rich layer forms when a Bioglass 45S5 surface is exposed an aqueous biological environment, which mineralizes to form hydroxycarbonate apatite and subsequently encourages the growth of bone.[2,7,9,11,12]

To tailor not only the bio-response but also the mechanical properties, composites of bioactive glass/ceramic materials and biocompatible polymers are required.[13] Bioactive glasses exhibit good biocompatibility and bio-functional performance but suffer from brittleness and low fracture strength.[14] In contrast, polymeric materials have a wide range of physical characteristics and may be readily processed into useful structures but are usually too flexible for load bearing applications.[3,15] Composites may be produced by combining bioglass particles with a polymer substrate, which exhibit better mechanical properties, such as higher stiffness and compressive strength, and therefore widen clinical usage.[3,15,16] PLGA/PDLLA and Bioglass 45S5 composites have been previously produced via thermally induced phase separation (TIPS) (Boccaccini et al.) and by dissolution in chloroform (Tsigkou et al.) but each only achieves an upper limit of ∼50 wt.% Bioglass 45S5 loading (∼30 vol.%).[17–23]

The low temperatures (<200°C) typically used during cold sintering allow polymers to be integrated with ceramics and glass in a manner not possible with conventional densification routes (>1000°C).[24–31] Tailoring of electrical, thermal, and mechanical properties of ceramics has already been demonstrated when composites are formed with polymers such as PTFE, PVDF-HFP, PEDOT:PSS, and PEI.[24,27–31] In this study, cold sintered bioglass–PLA (Polylactic acid) composites have been fabricated for the first time with up to 60 vol.% bioglass loading, 2× higher than reported by other fabrication routes. The cold sintered method is quick and simple, avoids the use of harmful solvents, may potentially be used to develop coatings through screen printing, and could be utilized to fabricate biomedical components with graded properties.[32,33] By varying the ratio of the end members, mechanical and bioactive properties may also be matched with surrounding tissues whilst encouraging bone growth and stronger, longer lasting implant fixation.

2 | EXPERIMENTAL PROCEDURES

Bioglass 45S5 powder was produced via a flame spray pyrolysis with a 1 M precursor solution of Na2-ethylhexanoate, hexamethyldisiloxane (HDMSO), Ca acetate hydrate, tributyl phosphate in the correct cation ratios for Bioglass 45S5 are add to a solvent composed of methanol/ethanol and 2-ethylhexanoic acid (2-eha). The solution is injected into the flame which results in rapid pyrolysis and the formation of powdered Bioglass 45S5. The average particle size (D_{50}) of the Bioglass 45S5 powder was found to be 14.9 μm, with significant agglomeration, leading to particle sizes up to 200 μm, whereas D_{50} of PLA powder is 116 μm.

2.1 | Cold sintering

Bioglass 45S5 powder was weighed and mixed in a pestle and mortar with 80 wt.% distilled water until homogenous. The wetted powder was transferred to a pressing die, and a uniaxial pressure of 250 MPa was then applied to the sample before heating to 100°C, with a dwell time of 60 min before cooling.

Bioglass 45S5 and PLA composites were produced by mixing the dry powders in a pestle and mortar and adding distilled water at 80 wt.% of the Bioglass 45S5 mass. Samples were again placed in a 0.5″ Ø die and pressed at 250 MPa before heating to 100°C for 60 min.

2.2 | X-ray diffraction

X-ray diffraction (XRD) was used to analyze powder and bulk samples after cold and conventional sintering. Diffraction data were obtained using a Bruker D2 Phaser (Karlsruhe, Germany) in Bragg–Brentano geometry with a Cu K_α radiation source ($\lambda = 1.5408$ Å), with 2.5° Soller slits and a 1 mm divergence slit at 30 kV and 10 mA. Data were collected across the 2θ range of 20°–60°.

Pellet samples were mounted in Bruker PMMA holders using Apiezon putty and to avoid height displacement errors, the surface flattened in-line with the top of the holder with a glass slide. Powder samples were placed into a zero-background holder and pressed using a glass slide to ensure that the specimen height was level with the holder.

2.3 | Scanning electron microscopy

Scanning electron microscopy (SEM) and energy-dispersive spectroscopy (EDS) were performed using an Inspect F50 (FEI, Hillsboro, Oregon, USA) operating with spot sizes of 3.00 and 5–10 kV. Samples were sputter coated with Au using an Agar AGB7340 Manual sputter coater to prevent charging.

2.4 | Nuclear magnetic resonance and Raman spectroscopy

NMR and Raman spectroscopy were performed on as-received, "wetted," and cold sintered bioglass samples. Wetted samples were analyzed to understand changes at each stage of the cold sintering process and were produced by mixing powder with distilled water (80 wt.%) in a pestle and mortar until homogenous.

The ^{29}Si MAS (magic-angle-spinning) NMR data used in this study were acquired at 7.05 T using a Varian-Chemagnetics Infinity-Plus 300 spectrometer operating at a ^{29}Si and ^{1}H Larmor frequencies (ν_0) of 59.6 and 300.13 MHz, respectively. Both single pulse (Bloch decay) ^{29}Si MAS NMR and ^{1}H–^{29}Si CPMAS (cross polarization, magic-angle-spinning) NMR experiments were performed using a Bruker 7 mm HX (dual channel) probe which enabled an MAS frequency of 5 kHz to be implemented. The ^{29}Si pulse length calibration was performed on solid kaolinite ($Al_2O_3 \cdot 2SiO_2 \cdot 2H_2O$) from which a $\pi/2$ pulse time of 4.5 μs was measured. All single pulse ^{29}Si MAS NMR data were measured with a $\pi/4$ pulse time of 2.25 μs, a recycle delay of 240 s, and a ^{1}H decoupling field of 80 kHz during data acquisition. The corresponding ^{29}Si CPMAS NMR measurements were undertaken using an initial ^{1}H $\pi/3$ pulse time of 3 μs, a ^{1}H–^{29}Si contact duration of 5 ms, a recycle delay of 20 s, and a ^{1}H decoupling field of 80 kHz during data acquisition. All reported 29Si chemical shifts were externally referenced against the IUPAC recommended primary reference of Me4Si (1% in CDCl3, $\delta = 0.0$ ppm) via the secondary solid kaolinite reference ($\delta = -92$ ppm).[34]

The accompanying single pulse ^{31}P MAS NMR and ^{1}H–^{31}P CPMAS NMR data were acquired at 11.7 T using a Bruker Avance III-500 spectrometer operating at the ^{31}P and ^{1}H Larmor frequencies (ν_0) of 202.4 and 500.13 MHz, respectively. These experiments were undertaken using a Bruker 3.2 mm HX (dual channel) probe that enabled an MAS frequency of 20 kHz to be implemented. The ^{31}P pulse length calibration was performed on solid ammonium dihydrogen phosphate ($(NH_4)H_2PO_4$) from which a $\pi/2$ pulse time of 3 μs was measured. All single pulse ^{31}P MAS NMR measurements were undertaken using a

TABLE 1   Mass and approximate volume fractions of PLA and bioglass in the composite samples

	PLA		Bioglass	
	Mass%	Vol.%	Mass%	Vol.%
A	100	100	0	0
B	80	90	20	10
C	75	87	25	13
D	60	77	40	23
E	50	69	50	31
F	30	49	70	51
G	25	42	75	58
H	0	0	100	100

$\pi/3$ pulse time of 2 μs, a recycle delay of 45 s, and a ^{1}H decoupling field of 100 kHz during data acquisition, whereas the corresponding ^{1}H–^{31}P CPMAS NMR data were measured using an initial ^{1}H $\pi/2$ pulse length of 3 μs, a ^{1}H–^{31}P contact duration of 5 ms (consisting of a CP ramp from 50%–100%), a recycle delay of 10 s and a ^{1}H decoupling field of 100 kHz during data acquisition. The reported ^{31}P chemical shifts were externally referenced against the IUPAC recommended primary reference of 85% H_3PO_4 ($\delta = 0.0$ ppm) via the secondary solid $(NH_4)H_2PO_4$ reference ($\delta = 0.99$ ppm).[34]

Raman spectra were collected on as-received powder, wetted powder, and cold sintered material. Raman spectra were obtained using an inVia Raman microscope (Renishaw, UK), equipped with a 514 nm laser. The laser power was 20 mW, and the acquisition time was 10 s with 30 acquisitions. Spectra were collected in the range of 200–1200 cm^{-1} where the main peaks associated with silicate and phosphate species are expected.[35–37]

2.5 | Cell culture assays

Cytotoxicity tests were performed on cold-sintered PLA–Bioglass 45S5 composites (as indicated in Table 1) with samples compared to tissue culture plastic (TCP). Human osteosarcoma cells (MG-63) from passages 15 to 20 were used and cultured in Minimum Essential Medium Eagle-Alpha Modification (αMEM) containing 100 IU/mL penicillin, 100 μg/mL streptomycin, 1% nonessential amino acids (all Sigma-Aldrich), and 10% fetal calf serum (Biosera).

Bioglass 45S5 and bioglass–PLA composite samples were sterilized by placing in 70% ethanol for 1 h then rinsing in sterile PBS three times. Preconditioning of bioglass samples is commonly utilized in the assessment of cytotoxicity, as in vitro testing is often performed in stationary systems and can be lead to unrepresentative results due to

high concentrations of alkali ions.[38] In this study, samples were pretreated for 7 days, incubated in fully supplemented αMEM with a change of media on Day 3. Samples were incubated on a Bibby Scientific rocking plate set at 45 rpm for 4 h to ensure mixing of the new medium. Following 7 days of pretreatment, MG-63 cells were seeded into a 6 well plate at 5.2×10^3 cells/cm^2. A transwell insert with a 0.4 μm membrane was inserted into the well. The samples were removed from medium, washed thrice with sterile PBS, and placed into the inserts. Fresh medium was then added to cover the bioglass. Transwells without bioglass or composite samples were used as TCP controls. Transwells and cold sintered Bioglass 45S5 pellets were also added to wells with no cells for normalization. After incubation for 24, 72, and 168 h, the transwells containing the Bioglass 45S5 were moved and washed with PBS. The MG-63s were imaged using a phase contrast microscope (Motic AE2000), and resazurin reduction assays were used to measure metabolic activity with cells washed with PBS and incubated in resazurin sodium salt (25.1 μg/mL) for 4 h. Samples of the resazurin media were then read in a fluorescence plate reader (excitation = 540 nm, emission 635 nm).

Values from wells containing no cells were subtracted from the other values to leave a no cell value of 0 and values normalized to the control on Day 1. Prism 7 (GraphPad) was used to perform all statistical analysis, unless otherwise stated. Statistical significance was defined as $p \leq .05$. Standard deviation was used for all error bars. Statistical significance was determined using two-way analysis of variance tests, with Dunnett's multiple comparison tests used to determine the significance between each Bioglass 45S5 group and the control.

3 | RESULTS

3.1 | Cold sintering of bioglass

Pellets produced via cold sintering were mechanically stable, with good handling characteristics and relative density of ∼95%, measured based on a theoretical density of 2.7 g/cm^3.[2,39] Densities were obtained using the geometric method as the Archimedes method is unreliable due to dissolution of the Bioglass. Surface structures are influenced by the contact surface with the die faces, with any scratches or indentation being transferred (as seen in Figure 1A). Fracture surfaces of cold sintered bioglass (Figure 1D–F) indicate that the microstructure is not homogenous, with more compacted regions of diameter 5–10 μm surrounded by finer grains. The regions that appear denser are tightly

packed agglomerated particles, likely retained from the starting powder.

XRD patterns of Bioglass 45S5 pellets (Figure 2A) indicate that the material remains amorphous after densification via cold sintering. SEM images reveal a largely pore-free microstructure, consistent with a relative density of ∼95%. Whisker-like structures are present on internal fracture surfaces. According to EDS, the whisker-like structures have elevated levels of calcium and phosphorus compared to the surrounding material (Figure 2E)[40–42] and are most likely composed of hydroxycarbonate apatite (see Section 3.5). Hydroxycarbonate apatite is a crucial stage of the interfacial reactions seen in bioglasses and is the foundation for promotion of bone growth.[2,7,9,11,12] It is proposed that when the powder is wetted prior to cold sintering, soluble ions leach from the material, which upon sintering at elevated temperature and pressure form hydroxycarbonate apatite in a process similar to that seen at lower temperatures and pressures within the body, albeit more rapidly.

3.2 | Cold sintering of PLA–Bioglass 45S5 composites

Optical images (Figure 3) show the surface of bioglass/PLA composites after cold sintering. The pellets were mechanically stable and component materials well distributed within samples.

Figure 4 shows SEM of the composite sample surfaces, which display regions of both the polymer and Bioglass 45S5 phases. In the 100 wt.% PLA samples, the surface is smooth with a low prevalence of pores. At the sintering temperature, the polymer particles have softened, and the applied pressure allows for a well densified material. As the concentration of Bioglass 45S5 is increased, isolated regions are seen on the surface similar in size to the agglomerates in the as-received material. Smaller particles of Bioglass 45S5 are also attached to the surface of PLA particles.

Fracture surfaces of the composites shown in Figure 5 also aid the understanding of the interaction between the two component materials. The internal microstructure of the 100 wt.% PLA (Figure 5A) shows that the particles have bonded together well, and there is very low porosity. With increasing Bioglass 45S5 content, as with the pellet surface, distinct regions of PLA and Bioglass 45S5 can be seen on the fracture surface (Figure 5C,E,G). In Figure 5G, where Bioglass 45S5 accounts for 60 vol.% of the pellet, the interface between the two materials is distinct but the particles of Bioglass 45S5 appear well-adhered to the PLA surface.
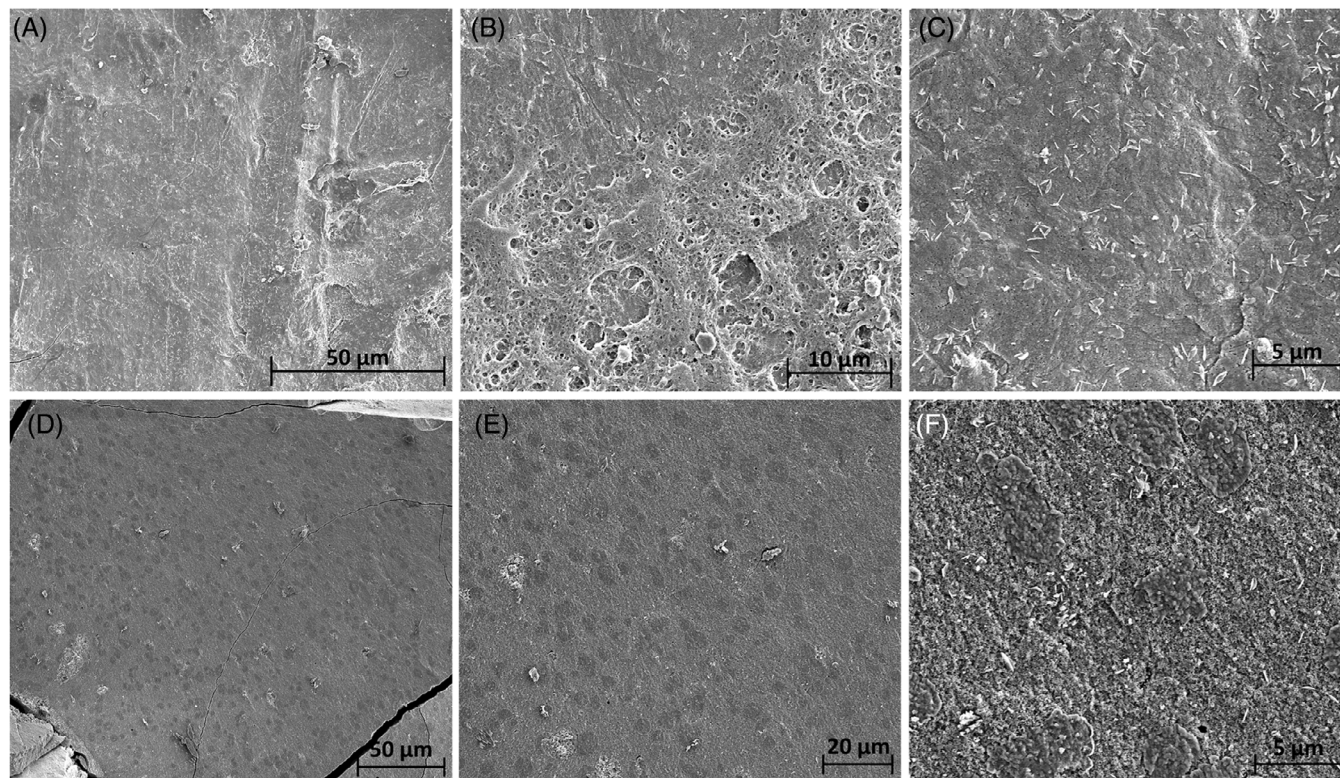
FIGURE 1 Scanning electron microscopy (SEM) images of pellet surface (A–C) and internal fracture surface (D–F) of cold sintered Bioglass 45S5. Surface shows low levels of porosity and some texture related to the surface finish cold sintering die. The internal structure shows some inhomogeneity with agglomerated particles thought to contribute to denser regions in the material.

A major advantage of the TIPS process to produce scaffolds is the ability to control the porosity and final structure by altering processing parameters.[22] From SEM images of the composites (Figures 4 and 5), the final microstructure appears to be mainly influenced by the morphology of the particles of the constituent materials. The PLA particles form distinct regions surrounded by Bioglass. The wetted Bioglass 45S5 powder forms a layer around the PLA on mixing and is then forced into gaps between polymer clusters under applied pressure. Homogeneity at shorter scales could be improved by reducing the PLA particle size to be more comparable with the Bioglass 45S5 powder. This also suggests that if more complex, tailored microstructures are desired, this could be achieved by utilizing alternative polymer particle morphologies. In addition, the pressure, time, and temperature of the cold sintering process may be varied to control the porosity level if required.

3.3 | Cell culture assays

Figure 6 shows the metabolic activity in the presence of the composite samples, after three sets ($N = 3$) of tests using three samples ($n = 3$) at each composition, normalized to the TCP values at Day 1. The red, dotted line in Figure 6 indicates 70% of the control metabolic activity measured in the TCP well, which is taken as the level at which the material is not cytotoxic.[43]

After 1-day incubation, the metabolic activity of indirectly seeded cells in the presence of PLA composite samples with 0–75 wt.% Bioglass 45S5 was at a comparable level to the TCP, whereas the 100% Bioglass 45S5 sample shows a 70% reduction in activity.

Over the course of the study, the metabolic activity in the TCP control samples increases, indicating the proliferation of cells, which was seen in optical images of the cells (Figure 7) where cell density increased over time. The metabolic activity recorded at Day 3 for cells incubated in the presence of PLA and composites with 25 and 50 wt.% Bioglass 45S5 was slightly lower than those incubated with TCP alone but are within 10%. A reduction of approximately 45% in the metabolic activity is seen in the 75 wt.% composite at Day 3. In the 100 wt.% Bioglass 45S5 samples, the metabolic activity reduced to approximately 10% of the TCP control values.

Similar trends were observed at Day 7, with cold sintered composites containing 0–75 wt.% Bioglass 45S5 all displaying good levels of activity compared to controls with all metabolic activity for all samples lying within 10% of
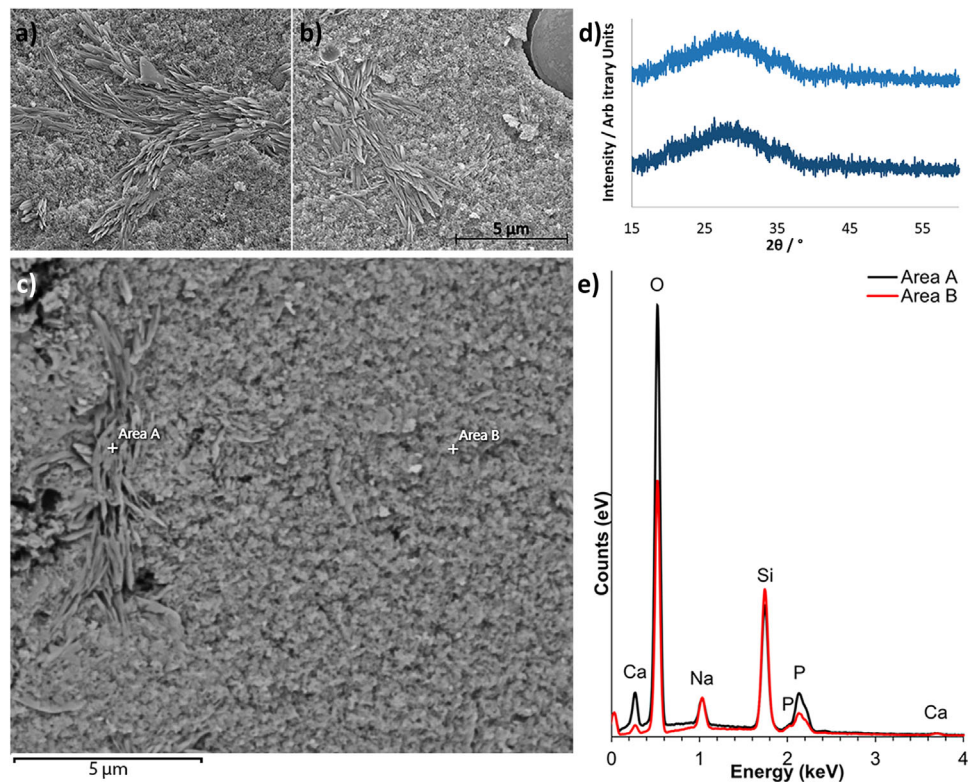
FIGURE 2 (A–C) Scanning electron microscopy (SEM) images of HCA-like structure on fracture surface of cold sintered bioglass pellets, scale bars 5 μm (A and B at same magnification), (D) X-ray diffraction (XRD) of as-received and cold sintered, and (E) energy-dispersive spectroscopy (EDS) of areas A and B indicated in (C).
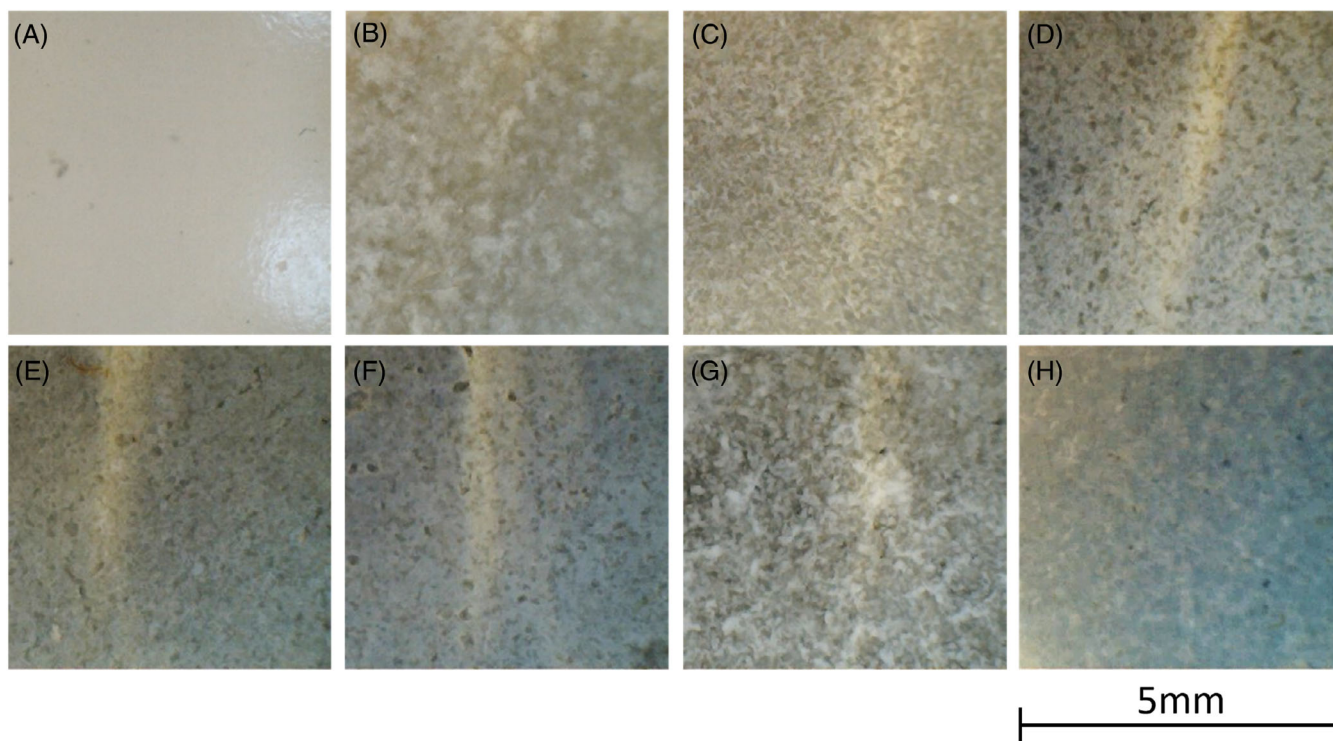

FIGURE 3 Optical images of cold sintered composite surfaces, with PLA:bioglass mass ratio (A) 100:0, (B) 80:20, (C) 75:25, (D) 60:40, (E) 50:50, (F) 30:70, (G) 25:75, and (H) 0:100.
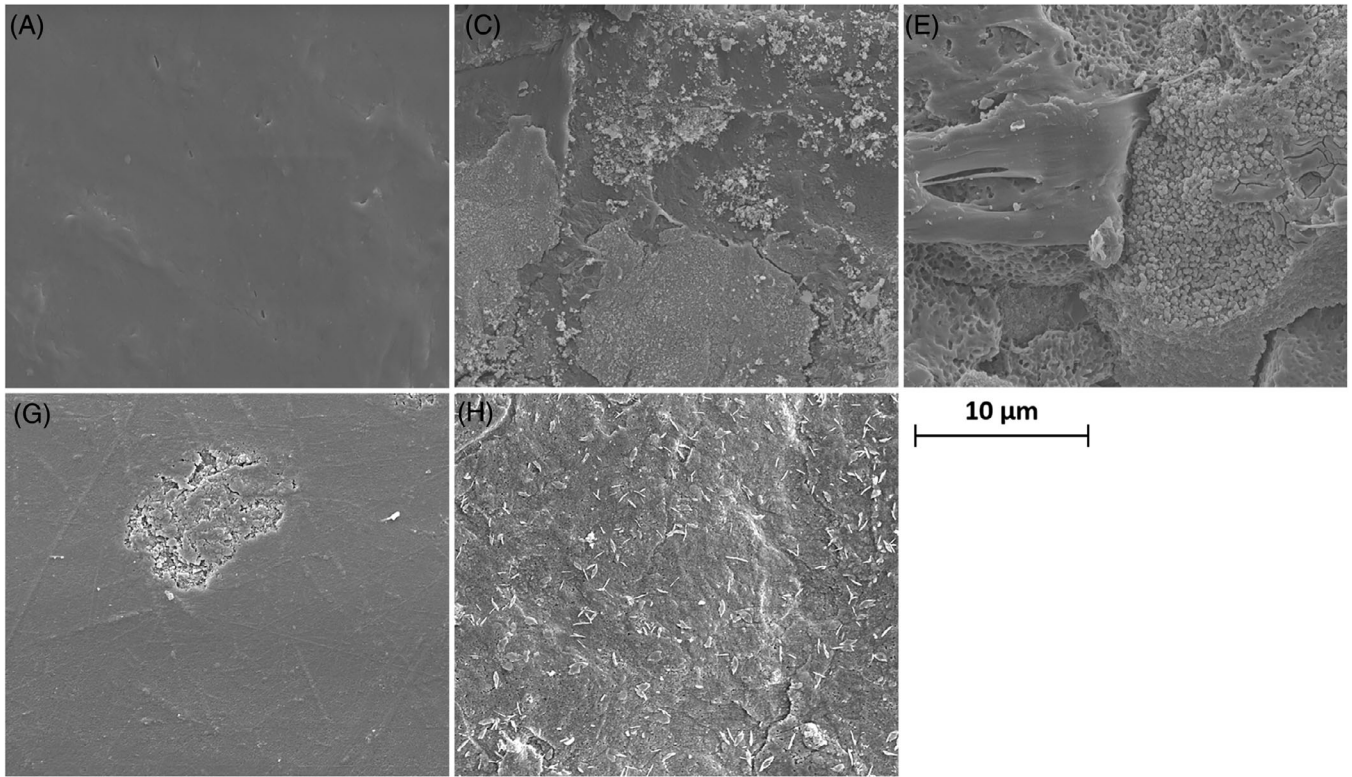
FIGURE 4   Scanning electron microscopy (SEM) of composite pellet surfaces. Inset figure labels are consistent with those in Table 1.
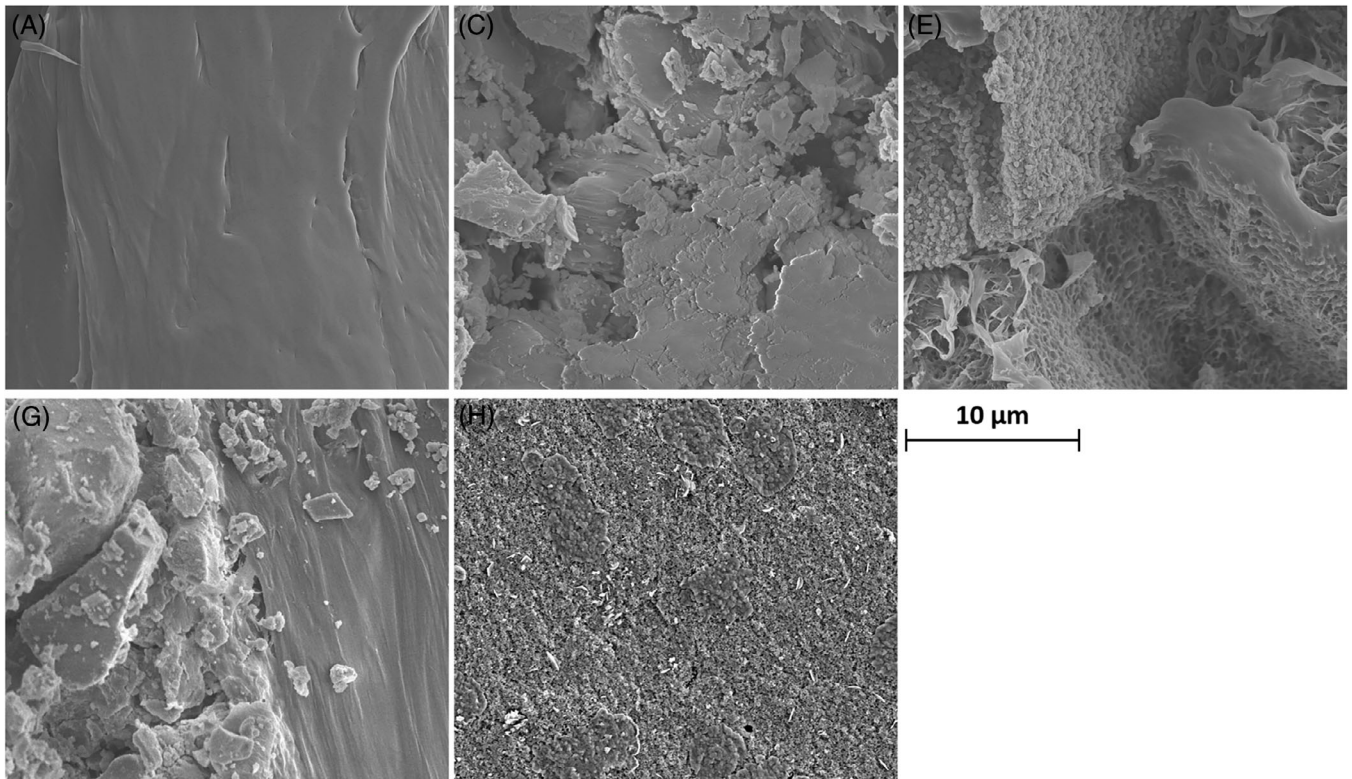

FIGURE 5   Scanning electron microscopy (SEM) of internal fracture surface of PLA (A), bioglass (H), and composite pellets (C, E, and G). Inset figure labels are consistent with those in Table 1. Areas of PLA are indicated with white arrows, whereas bioglass regions are indicated by black arrows.
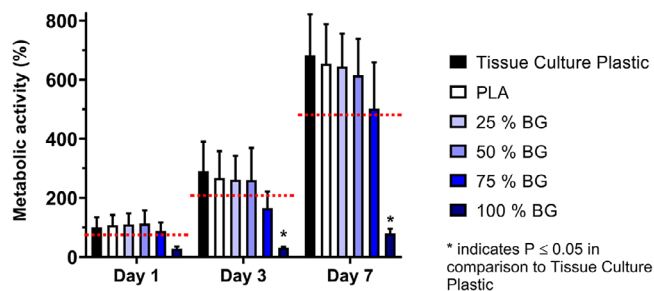
FIGURE 6 Metabolic activity at Days 1, 3, and 7 for composite samples, where % BG represents the percentage of Bioglass 45S5 in the as produced composites.

TCP. Samples with 75 wt.% showed approximately 80% viability compared to the control. At Day 7, the 100 wt.% cold sintered composite samples again show a significant reduction in the metabolic activity to around 10% of the control.

Optical images (Figure 7) of indirectly seeded cells agree well with the metabolic activity. The number of cells observed on all plates increased over time, and the presence of a bright "halo" around a cell indicates that it has detached from the cell plate and is therefore either dividing or dead.

Results after Day 1 of cytotoxicity testing showed a metabolic activity range for 0–75 wt.% samples, 90%–110% of that observed in the TCP with all above the activity level which indicates that the samples are noncytotoxic. The reduction in metabolic activity for 100 wt.% Bioglass 45S5 was likely due to higher levels of leachable ions present which remain at high levels after pretreatment. These ions will continue to be released during the incubation period and contribute to the reduction in metabolic activity due to an increase in pH of the media. For this reason, pretreatment of these materials before in vitro testing is often performed,[44] and here, we used a 7-day pretreatment to stabilize the release of leachable ions into the media during testing to ensure the pH stayed within a physiological range and remained suitable for the cell lines used. Indirect cell seeding also significantly improved the observed metabolic activity compared to direct seeding (not shown) as the well plate surface is smoother than the composite samples and allowed for the imaging of cells to assess morphology and proliferation.

The morphologies of cells seen in Figure 7 are typical MG-63 cells[45–47] and have become so confluent for composite samples with up to 75 wt.% Bioglass 45S5 at Day 7 that the precise morphology is no longer discernible. In 100 wt.% Bioglass 45S5 samples, low proliferation of cells at Days 1 and 3 agrees with the low metabolic activity data. At Day 7, the metabolic activity increases, and the cell coverage increases, with a reduction in the proportion of cells

which are surrounded by "halos" indicating that rate of cell death may have reduced. This may relate to a reduction in concentration of alkali ions in the transwells after rinsing at each metabolic activity testing timepoint.

3.4 | Speciation of wetted and sintered Bioglass 45S5 and its role in the densification and bioactive response

To understand the mechanism of the cold sintering process and how it affects the Bioglass 45S5 structure, ^{29}Si and ^{31}P MAS NMR measurements were also performed on wetted and sintered material (see Figure 8). Both CPMAS and single pulse excitation, MAS techniques were used to study the Si and P speciation in this suite of Bioglass 45S5 preparations. The CPMAS measurements should, in principle, enhance the signal-to-noise of those P and Si positions proximate to protonated species such as OH and H_2O groups; however, a comparison of the acquired CPMAS and MAS data for each nucleus demonstrates that these is little change, suggesting that the proton network is homogeneous throughout the Bioglass 45S5 structural networks. Furthermore, the signal-to-noise from both ^{31}P and ^{29}Si CPMAS measurements is comparable, and sometimes less that obtained from the ^{31}P and ^{29}Si MAS counterparts indicating that these protonated species are mobile and thus modulate the ^{1}H–^{31}P and ^{1}H–^{29}Si heteronuclear dipolar interactions required for efficient CP contact and signal enhancement. The single pulse MAS measurements are quantitative and have been used to determine the formal distribution of the P and Si Q speciation comprising these systems. Deconvolution of the ^{31}P CPMAS and MAS NMR data shown in Figure 8A,B indicates that three P species are observed in the ~3–8 ppm chemical shift range signifying Q^1 speciation (possessing one bridging O) in all cases. The observed ^{31}P chemical shifts of these Q^1 species will be influenced by their proximity to other bridging and non-bridging O species, as well as network modifiers such as Ca, thus resulting in a chemical shift distribution. Upon wetting, the incorporation of H_2O within Bioglass 45S5 network is identified the appearance of an additional P species appears at ~0 ppm, with all ^{31}P resonances shifting to lower frequency by ~2 ppm. This wetting process is largely reversible as subsequent the sintering and removal of free water is associated with the return of the ^{31}P chemical shifts to their initial positions (Figure 8A,B), although a small change within the final Q^1 species distribution is observed.

Figure 9 shows how the proportions of phosphorus Q_1 species are affected by the stages of cold sintering. The addition of distilled water to the "wetted" samples promotes the formation of phosphate species, not seen in the
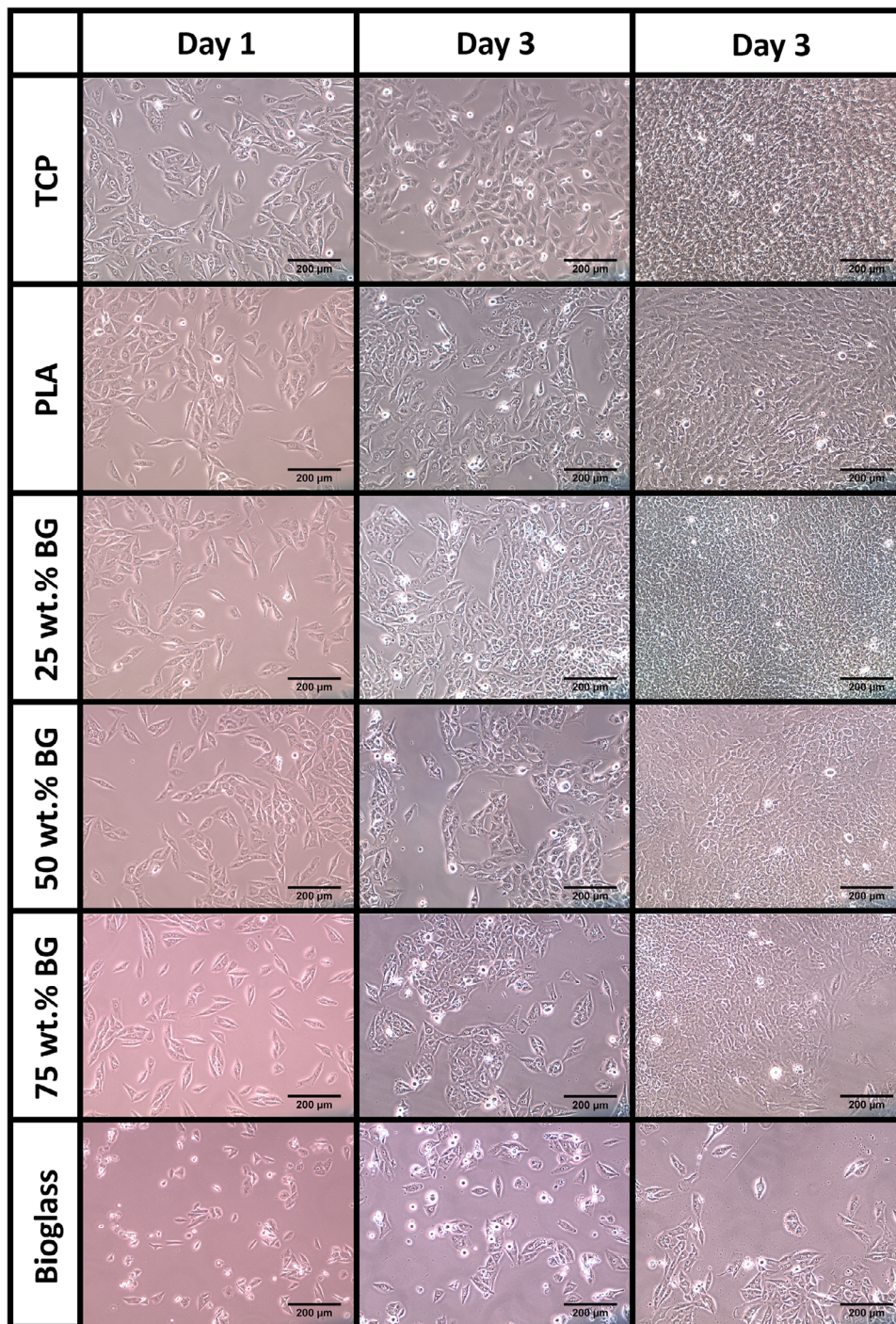
FIGURE 7 Optical micrograph of cells after 1-, 3-, and 7-days indirect incubation, where % BG represents the percentage of Bioglass 45S5 in the as produced composites.

as-received and sintered material. The proportion of all phosphate species changes during the cold sintering process but is similar between as-received and final sintered samples.

Figure 10 shows how the proportion of the Q^n silica species, as determined from the ^{29}Si MAS NMR (Figure 8D), changes during the cold sintering process. The powder wetted with 80 wt.% distilled water shows a significant decrease in Q^3 species, whereas all other species increase. After cold sintering, the proportion of Q^2 species continues to increase. Q^1 and Q^4 species decrease after sintering to levels below those seen in the as-received powder. The amount of Q^3 species increases but recovers to the level of the as-received powder. The overall Si network connectivity is shown to reduce when the powder is wetted and then increases after the materials are sintered.
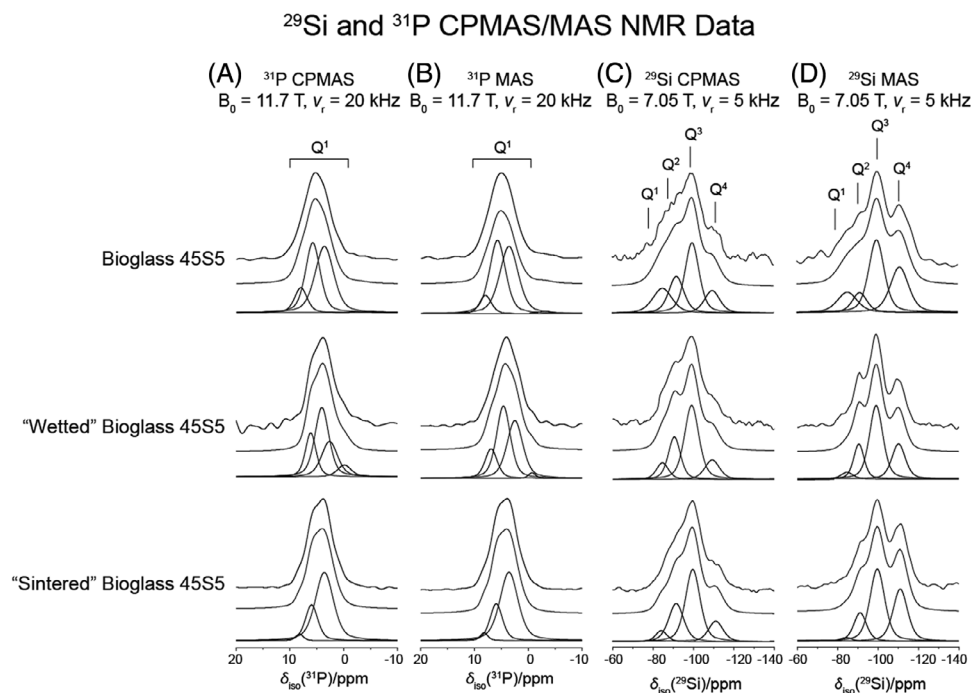
^{29}Si and ^{31}P CPMAS/MAS NMR Data

FIGURE 8 The 29Si and 31P cross polarization, magic-angle-spinning (CPMAS)/magic-angle-spinning (MAS) NMR data for Bioglass 45S5, "wetted" Bioglass 45S5, and "sintered" Bioglass 45S5. (A) ^{31}P CPMAS, (B) ^{31}P MAS, (C) ^{29}Si CPMAS and (D) ^{29}Si MAS

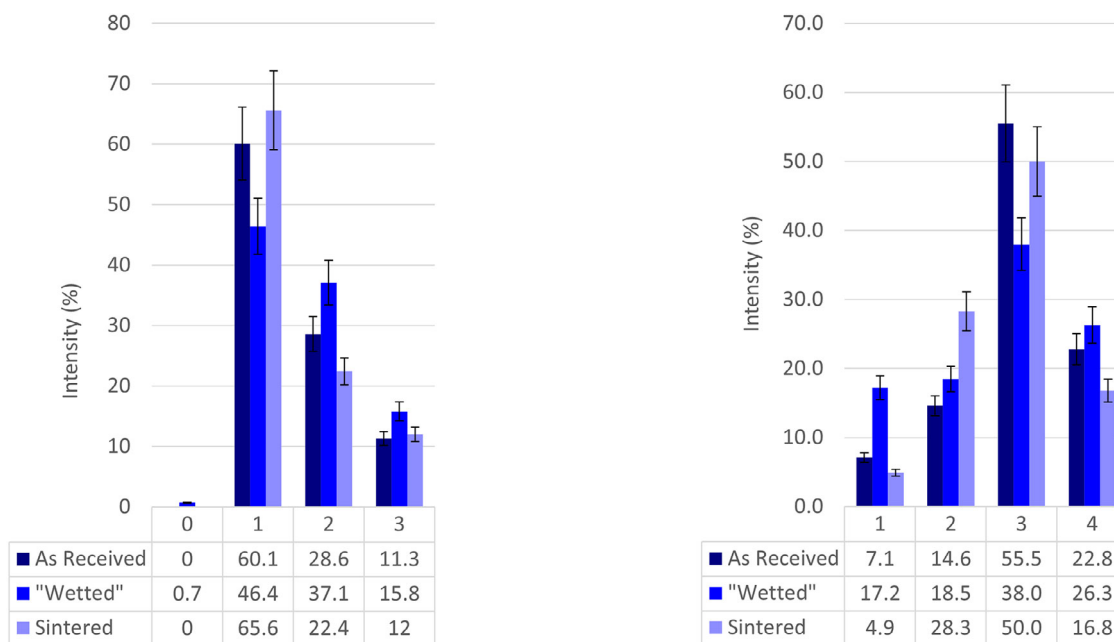|	0	1	2	3
As Received	0	60.1	28.6	11.3
"Wetted"	0.7	46.4	37.1	15.8
Sintered	0	65.6	22.4	12

FIGURE 9 The percentage of Q1 species as determined from the 31P magic-angle-spinning (MAS) NMR data of as-received, wetted, and sintered Bioglass 45S5 powder.

	1	2	3	4
As Received	7.1	14.6	55.5	22.8
"Wetted"	17.2	18.5	38.0	26.3
Sintered	4.9	28.3	50.0	16.8

FIGURE 10 The percentages of Q species as determined from the 29Si magic-angle-spinning (MAS) NMR data of as-received, wetted, and sintered Bioglass 45S5 powder.

The increase in the proportions of Q^1 and Q^2 species in wetted powder corresponds with an increase in non-bridging oxygens, indicating a reduction in connectivity of the network. This is attributed to breaking Si–O–Si bonds and the formation of Si–O–H bonds. These changes

are analogs to the mechanism proposed in the second stage of the interfacial reactions of Bioglass 45S5 during implantation.[2,7,9,11,12] As soluble alkali ions are dissolved into the water from the powder, they no longer act as network modifiers within the glass structure, creating a
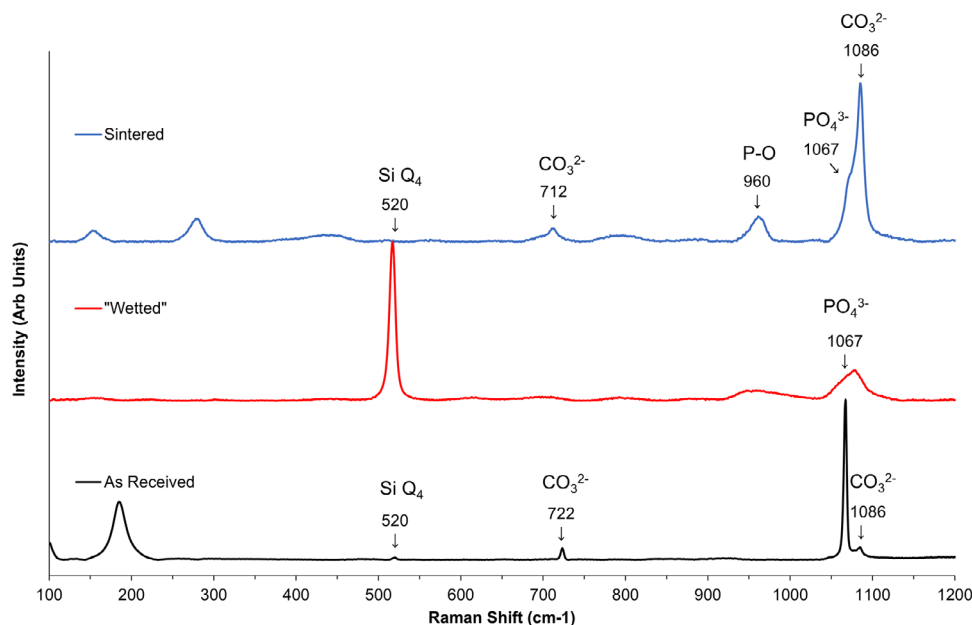
FIGURE 11   Raman spectra of as-received, wetted, and sintered Bioglass 45S5 powder.

solution with a higher pH, which contributes to enhanced dissolution of the silica network. The increase in the fully condensed Q^4 species in the wetted material is indicative of the formation of a silica-rich region due to the loss of alkali ions from the powder surface with condensation reactions leading to the formation of Si–O–Si bonds.

These changes in Si species agree with the proposed stages of interfacial reactions observed during the formation of bonding between bioactive glasses and bone.[2,7,9,11,12] In stage 4 of these interfacial reactions, PO_4^{3-} and Ca^{2+} ions are adsorbed from the Bioglass 45S5 and surrounding media, creating an amorphous layer of $CaO–P_2O_5$ on the silica-rich surface. This amorphous calcium phosphate layer subsequently crystallizes in the fifth reaction stage to form HCA.

3.5 | Raman spectroscopy

To understand further the changes occurring within the structure of the bioglass powder during cold sintering, Raman spectra were collected on as-received powder, wetted powder, and cold sintered pellets (Figure 11).

At 520 cm^{-1}, the intense mode in the wetted powder sample and the small intense band in the as-received powder are attributed to Si Q_4 species. This agrees well with the Si NMR, which indicates an increase in Q_4 species in the wetted material but which reduces after cold sintering.

The peaks at 722 cm^{-1} in the as-received sample and 712 cm^{-1} in the cold sintered are attributed to CO_3^{2-}.[37,48] In the as-received powder, this is likely to be due to adsorption

of CO_2 onto the surface of the powder and to carbonated hydroxyapatite in the sintered pellet.

Raman spectra for the cold sintered sample show a band at ~960 cm^{-1} which can been attributed to symmetric stretching of P–O bond, a characteristic peak associated with carbonated hydroxyapatite.[35,48–52] Raman peaks observed below ~310 cm^{-1} have previously been attributed to Ca^{2+} and PO_4^{3-} in hydroxyapatite.[53] The broad peak between 400 and 475 cm^{-1}, although not well resolved, might be attributable to bending vibrations within PO_4^{3-} tetrahedra. This agrees with EDX of the fracture surface of cold sintered bioglass which indicates the likely presence of carbonated hydroxyapatite. Evidence of this phase is not seen in the XRD data (a bulk technique) due to its low volume fraction but is detected by Raman as it is a surface characterization technique. Its presence is a positive indication of potential bioactivity.

Modes are seen in all samples between ~1050 and 1100 cm^{-1} whose intensities vary. Modes in the 1060–1080 cm^{-1} range are commonly attributed to v_3 phosphate species,[37,48,52,54] whereas those at ~1086 cm^{-1} are associated with carbonate groups. Kane et al. indicated that a Raman shift of 1079–1080 cm^{-1} may be assigned to amorphous potassium carbonate.[55] The intensity of these modes increases in the sintered pellet compared to as-received powder and further indicates the formation of carbonated hydroxyapatite within the cold sintered samples.[35,37,48] In the wetted sample, the mode in the 1050–1100 cm^{-1} range is broad and could be ascribed to a number of different structural groups, such as phosphates and carbonates,
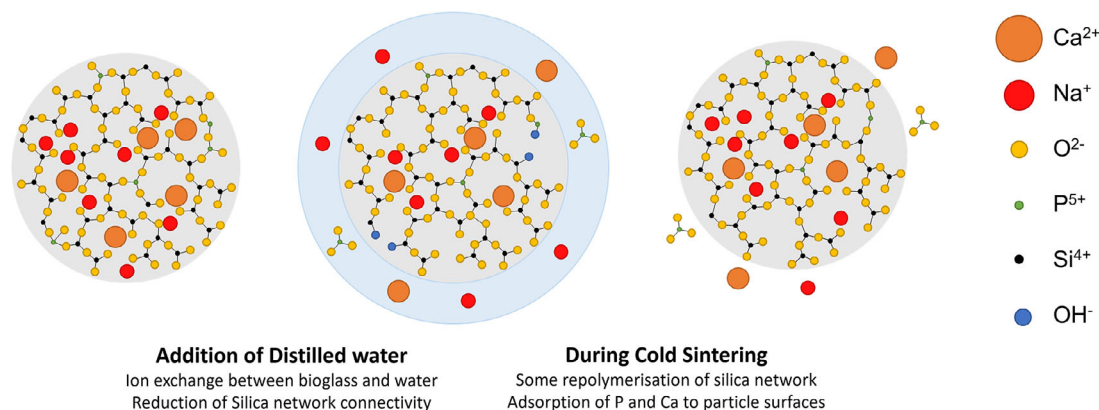
Addition of Distilled water
Ion exchange between bioglass and water
Reduction of Silica network connectivity

During Cold Sintering
Some repolymerisation of silica network
Adsorption of P and Ca to particle surfaces

FIGURE 12 Schematic representation of the proposed mechanisms seen during the cold sintering of Bioglass 45S5.

detected in the as-received powder and cold sintered pellet.

4 | CONCLUSIONS

Densification of Bioglass 45S5 at temperatures significantly lower than T_g using the cold sintering process at 100°C with distilled water has been demonstrated for the first time. Changes in chemical structure of Bioglass 45S5 indicated by NMR and Raman spectroscopy before, "during," and after cold sintering have been studied, allowing the potential cold sintering mechanism to be revealed. XRD patterns of cold sintered Bioglass 45S5 confirm that the materials remain amorphous during sintering, whereas Ca- and P-rich whiskers are observed in SEM images of the surface.

Structural changes observed from NMR are characterized by an initial reduction in the silica network connectivity with the addition of distilled water and a partial recovery of the network connectivity after the cold sintering stage. A reduction in silica network connectivity is expected in the wetted powder due to the creation of Si–OH bonds alongside the dissolution of alkali ions. Raman spectra generally confirm the NMR results with an increase in Si Q4 species in wetted samples and the presence of carbonate and phosphate species in as-received powder and cold sintered pellets. Based on NMR and Raman spectroscopy, we propose that hydroxycarbonate apatite forms during cold sintering and acts as part of the densification mechanism.

Bioglass 45S5 is designed to interact with fluids within the body and has a well-reported sequence of interfacial reactions. The inherent interactions of Bioglass 45S5 with body fluids during implantation appear closely related, although accelerated through temperature and pressure, to those responsible for cold sintering, as illustrated Figure 12.[2,7,9,11,12] The physical–chemical features of bioglasses vary significantly with composition and fabrication route. Although inherent dissolution behavior might indicate that all bioglasses can be densified through cold sintering, the mechanism and impact of the process on properties is likely to depend on composition.

The very low temperature involved in cold sintering Bioglass 45S5 (100°C) enables fabrication of bioactive components in a manner not previously reported. Not only can crystallization be avoided but Bioglass 45S5–polymer composites can be readily fabricated with 2× greater volume loading than by other methods. After standard preconditioning of the composites, the cytotoxicity of Bioglass 45S5–PLA composites in this study was promising and indicated that the cold sintering could be used to produce implant materials with tailored to physical properties. Mechanical properties and bioactivity have not been studied in this work, it will be necessary to understand how composites prepared through cold sintering compare with previously reported methods when considering potential future applications.

REFERENCES
1. Hench LL, Wilson J. Surface-active biomaterials. Science. 1980;226:630–6.
2. Hench LL. Bioceramics. J Am Ceram Soc. 1998;81:1705–1728.

3. Chen J, Shi W, Norman AJ, Ilavarasan P. Biomedical applications of polymer-composite materials: a review. Compos Sci Technol. 2001;6 (9):1189–224. https://doi.org/10.1109/isemc.2002.1032709

4. Oldani C, Dominguez A. Titanium as a biomaterial for implants. In: Recent advances in arthroplasty. IntechOpen. 2012.

5. Wang X, Nyman JS, Dong X, Leng H, Reyes M. Fundamental biomechanics in bone tissue engineering. In: Synthesis lectures on tissue engineering. Morgan & Crosspool. 2010.

6. Currey JD. Bones: structure and mechanics. Princeton University Press. 2013.

7. Gerhardt L-C, Boccaccini AR. Bioactive glass and glass-ceramic scaffolds for bone tissue engineering. Materials. 2010;3(7):3867–910. https://doi.org/10.3390/ma3073867

8. Hench LL. Biomaterials: a forecast for the future. Biomaterials. 1998;19:1419–23.

9. Leonor IB, Rodrigues AI, Reis RL. Designing biomaterials based on biomineralization for bone repair and regeneration. In: Biomineralisation and biomaterials. Amsterdam: Elsevier Ltd.; 2016. https://doi.org/10.1016/B978-1-78242-338-6.00014-4

10. Hench LL. The story of bioglass. J Mater Sci: Mater Med. 2006;17:967–78.

11. Hench LL. Opening paper 2015 – some comments on bioglass: four eras of discovery and development. Biomed Glasses. 2015;1:1–11.

12. Hench LL. Bioceramics: from concept to clinic. J Am Ceram Soc. 1991;74;1487–510.

13. Baino F, Hamzehlou S, Kargozar S. Bioactive glasses: Where are we and where are we going? J Funct Biomater. 2018;9(1):25.

14. Zahid S, Shah AT, Jamal A, Chaudhry AA, Khan AS, Khan AF, et al. Biological behavior of bioactive glasses and their composites. RSC Adv. 2016;6:70197–214.

15. Kaur G. Clinical applications of biomaterials. State-of-the-art progress, trends, and novel approaches. Cham: Springer International; 2017.

16. Boccaccini AR, Erol M, Stark WJ, Mohn D, Hong Z, Mano JF. Polymer/bioactive glass nanocomposites for biomedical applications: a review. Compos Sci Technol. 2010;70:1764–76.

17. Tsigkou O, Hench LL, Boccaccini AR, Polak JM, Stevens MM. Enhanced differentiation and mineralization bioglass composite films in the absence of human fetal osteoblasts on PDLLA containing of osteogenic supplements. J Biomed Mater Res, A. 2006;79:963–73.

18. Yang XB, Webb D, Blaker J, Boccaccini AR, Maquet V, Cooper C, et al. Evaluation of human bone marrow stromal cell growth on biodegradable polymer/Bioglass® composites. Biochem Biophys Res Commun. 2006;342:1098–107.

19. Blaker JJ, Maquet V, Jérôme R, Boccaccini AR, Nazhat SN. Mechanical properties of highly porous PDLLA/Bioglass® composite foams as scaffolds for bone tissue engineering. Acta Biomater. 2005;1:643–52.

20. Blaker JJ, Gough JE, Maquet V, Notinger I, Boccaccini AR. In vitro evaluation of novel bioactive composites based on Bioglass®-filled polylactide foams for bone tissue engineering scaffolds. J Biomed Mater Res, A. 2003;67:1401–11.

21. Boccaccini AR, Blaker JJ, Maquet V, Jerome R, Blacher S, Roether JA. Biodegradable and bioactive Polymer/Bioglass® composite foams for tissue engineering scaffolds. Mater Sci Forum. 2005;494:499–506.

22. Conoscenti G, Carrubba VLa, Brucato V. A versatile technique to produce porous polymeric scaffolds: the thermally induced phase separation (TIPS) method. Arch Chem Res. 2017;01:10–2.

23. Maquet V, Boccaccini AR, Pravata L, Notingher I, Jérôme R. Preparation, characterization, and in vitro degradation of bioresorbable and bioactive composites based on Bioglass®-filled polylactide foams. J Biomed Mater Res, A. 2003;66:335–46.

24. Guo J, Pfeiffenberger N, Beese A, Rhoades A, Gao L, Baker A, et al. Cold sintering $Na_2Mo_2O_7$ ceramic with poly(ether imide) (PEI) polymer to realize high-performance composites and integrated multilayer circuits. ACS Appl Nano Mater. 2018;1:3837–44.

25. Wang D, Zhou D, Song K, Feteira A, Randall CA, Reaney IM. Cold-sintered C0G multilayer ceramic capacitors. Adv Electron Mater. 2019;1900025:1–5.

26. Funahashi S, Guo H, Guo J, Baker AL, Wang Ke, Shiratsuyu K, et al. Cold sintering and co-firing of a multilayer device with thermoelectric materials. J Am Ceram Soc. 2017;100:3488–96.

27. Guo J, Berbano SS, Guo H, Baker AL, Lanagan MT, Randall CA. Cold sintering process of composites: bridging the processing temperature gap of ceramic and polymer materials. Adv Funct Mater. 2016;26(39):7115–21 https://doi.org/10.1002/adfm.201602489

28. Guo J, Zhao X, Herisson De Beauvoir T, Seo J-H, Berbano SS, Baker AL, et al. Recent progress in applications of the cold sintering process for ceramic-polymer composites. Adv Funct Mater. 2018;1801724:1801724.

29. Guo J, Guo H, Heidary DSB, Funahashi S, Randall CA. Semiconducting properties of cold sintered V2O5 ceramics and Co-sintered V2O5-PEDOT:PSS composites. J Eur Ceram Soc. 2016;26(39):1529–34 https://doi.org/10.1016/j.jeurceramsoc.2016.11.021

30. Guo J, Baker AL, Guo H, Lanagan M, Randall CA. Cold sintering process: a new era for ceramic packaging and microwave device development. J Am Ceram Soc. 2016;7:1–7.

31. Zhao Y et al. Cold-sintered V2O5-PEDOT:PSS nanocomposites for negative temperature coefficient materials. J Eur Ceram Soc. 2019;39:1257–1262. https://doi.org/10.1016/j.jeurceramsoc.2018.10.018

32. Baino F. Functionally graded bioactive glass-derived scaffolds mimicking bone tissue. In: Biomedical, therapeutic and clinical applications of bioactive glasses. Amsterdam: Elsevier Ltd.; 2019. p. 443–66. https://doi.org/10.1016/b978-0-08-102196-5.00016-1

33. Roop Kumar R, Wang M. Functionally graded bioactive coatings of hydroxyapatite/titanium oxide composite system. Mater Lett. 2002;55:133–7

34. Harris RK, Becker ED, Cabral De Menezes SM, Goodfellow R, Granger P. Nuclear spin properties and conventions for chemical shifts - IUPAC recommendations 2001. Solid State Nucl Magn Reson. 2002;22:458–83.

35. Seah RKH, Garland M, Loo JSC, Widjaja E. Use of Raman microscopy and multivariate data analysis to observe the biomimetic growth of carbonated hydroxyapatite on bioactive glass. Anal Chem. 2009;81:1442–9.

36. Rehman I, Karsh M, Hench LL, Bonfield W. Analysis of apatite layers on glass-ceramic particulate using FTIR and FT-Raman spectroscopy. J Biomed Mater Res. 2000;50(2):97–100. https://doi.org/10.1002/(SICI)1097-4636(200005)50:2⟨97::AID-JBM1⟩3.0.CO;2-7

37. Rehman I, Hench LL, Bonfield W, Smith R. Analysis of surface layers on bioactive glasses. Biomaterials. 1994;15:865–70.

38. Ciraldo FE, Boccardi E, Melli V, Westhauser F, Boccaccini AR. Tackling bioactive glass excessive in vitro bioreactivity: preconditioning approaches for cell culture tests. Acta Biomater. 2018;75:3–10.

39. Jones JR. Review of bioactive glass: from Hench to hybrids. Acta Biomater. 2013;9:4457–86.

40. Liu J, Ye X, Wang H, Zhu M, Wang Bo, Yan H. The influence of pH and temperature on the morphology of hydroxyapatite synthesized by hydrothermal method. Ceram Int. 2003;29:629–33.

41. Chen C, Huang Z, Yuan W, Li J, Cheng X, Chi Ru-An. Pressure effecting on morphology of hydroxyapatite crystals in homogeneous system. CrystEngComm. 2011;13:1632–7.

42. Neira IS, Kolen'ko YV, Lebedev OI, Tendeloo GV, Gupta HS, Guitian F, et al. An effective morphology control of hydroxyapatite crystals via hydrothermal synthesis. Cryst Growth Des. 2009;9(1):466–74.

43. British Standards Institution. Biological evaluation of medical devices. EN ISO 1099-3-5. 2009;26.

44. Hohenbild F, Arango-Ospina M, Moghaddam A, Boccaccini AR, Westhauser F. Preconditioning of bioactive glasses before introduction to static cell culture: what is really necessary? Methods Protoc. 2020;3:1–12.

45. Price N, Bendall SP, Frondoza C, Jinnah RH, Hungerford DS. Human osteoblast-like cells (MG63) proliferate on a bioactive glass surface. J Biomed Mater Res. 1997;37:394–400.

46. Ahmed I, Cronin PS, Abou Neel EA, Parsons AJ, Knowles JC, Rudd CD. Retention of mechanical properties and cytocompatibility of a phosphate-based glass fiber/polylactic acid composite. J Biomed Mater Res, B. 2009;89:18–27.

47. Variola F, Vetrone F, Richert L, Jedrzejowski P, Yi Ji-H, Zalzal S, et al. Improving biocompatibility of implantable metals by nanoscale modification of surfaces: an overview of strategies, fabrication methods, and challenges. Small. 2009;5:996–1006.

48. Popa A-C, Stan G, Husanu M-A, Mercioniu I, Santos L, Fernandes H, et al. Bioglass implant-coating interactions in synthetic physiological fluids with varying degrees of biomimicry. Int J Nanomed. 2017;12:683–707.

49. Shaikh S, Kedia S, Majumdar AG, Subramanian M, Sinha S. 45S5 bioactive glass coating on Ti6Al4V alloy using pulsed laser deposition technique. Mater Res Express. 2019;6(12).

50. Michelot A, Sarda S, Audin C, Deydier E, Manoury E, Poli R, et al. Spectroscopic characterisation of hydroxyapatite and nanocrystalline apatite with grafted aminopropyltriethoxysilane: nature of silane–surface interaction. J Mater Sci. 2015;50:5746–57.

51. Kishore Chakraborty P, Jaideep Adhikari AB, Saha P. Variation of the properties of sol-gel synthesized bioactive glass 45S5 in organic and inorganic acid catalysts. Mater. Adv. 2021;2:413.

52. de Aza PN, Guitián F, Santos C, de Aza S, Cuscó R, Artús L. Vibrational properties of calcium phosphate compounds. 2. Comparison between hydroxyapatite and β-tricalcium phosphate. Chem Mater. 1997;9:916–22.

53. Iqbal Z, Tomaselli VP, Fahrenfeld O, Möller KD, Ruszala FA, Kostiner E. Polarized Raman scattering and low frequency infrared study of hydroxyapatite. J Phys Chem Solids. 1977;38:923–7.

54. Londoño-Restrepo SM, Zubieta-Otero LF, Jeronimo-Cruz R, Mondragon MA, Rodriguez-García ME. Effect of the crystal size on the infrared and Raman spectra of bio hydroxyapatite of human, bovine, and porcine bones. J Raman Spectrosc. 2019;50:1120–9.

55. Kane SN, Mishra A, Dutta AK. Spectral analysis of allogeneic hydroxyapatite powders. J Phys Conf Ser. 2016;755(1).